Numerical Analysis of Incipient Separation on 53º Swept Diamond Wing

Neal T. Frink[1]

NASA Langley Research Center, Hampton, Virginia 23681, USA

A systematic analysis of incipient separation and subsequent vortex formation from moderately swept blunt leading edges is presented for a 53⁰ swept diamond wing. This work contributes to a collective body of knowledge generated within the NATO/STO AVT-183 Task Group titled "Reliable Prediction of Separated Flow Onset and Progression for Air and Sea Vehicles". The objective is to extract insights from the experimentally measured and numerically computed flow fields that might enable turbulence experts to further improve their models for predicting swept blunt leading-edge flow separation. Details of vortex formation are inferred from numerical solutions after establishing a good correlation of the global flow field and surface pressure distributions between wind tunnel measurements and computed flow solutions. From this, significant and sometimes surprising insights into the nature of incipient separation and part-span vortex formation are derived from the wealth of information available in the computational solutions.

Nomenclature

C_f	=	skin friction coefficient
C_L	=	lift coefficient, $=\text{Lift}/q_\infty S_{ref}$
C_p	=	pressure coefficient
c_R	=	wing root chord, $=1.2$m
M_∞	=	freestream Mach number, $=0.15$
mac	=	mean aerodynamic chord, $=2/3*c_R=0.8$m
q_∞	=	dynamic pressure, N/m^2
Re_{mac}	=	Reynolds number based on mac, $=2.7$ million
$rate1$ & $rate2$	=	primary& secondary VGRID "viscous" stretching factors, see Eq. 1
S_{ref}	=	reference area, $=0.77$m^2
Δt	=	physical time step, seconds
Δt^*	=	characteristic time step, $=\Delta t \bullet U_\infty/mac$
U_∞	=	freestream velocity, m/s
α	=	angle of attack, deg.
δ_{i+1}	=	VGRID "viscous" grid spacing normal to surface at node $i+1$, see Eq. 1, meter
δ_1	=	spacing of first node off of surface in "viscous" grid layers, see Eq. 1, meter

<u>Key Acronyms</u>

AVT	=	Applied Vehicle Technology
CFD	=	Computational Fluid Dynamics
HWA	=	Hot-wire anemometry
KE, k-ε	=	Jones-Launder linear k-epsilon two equation turbulence model
LE	=	Leading edge of diamond wing
NATO/STO	=	North Atlantic Treaty Organization / Science and Technology Organization
PIV	=	Particle image velocimetry
RANS	=	Reynolds Averaged Navier Stokes
SA	=	Spalart-Allmaras one equation turbulence model
SACCON	=	Stability and Control Configuration
SST	=	Menter's Shear Stress Transport two equation turbulence model

---

[1] Senior Researcher, Configuration Aerodynamics Branch, Research Directorate, MS 499, Associate Fellow, AIAA

ST   = Streamtrace
TKE   = Turbulent kinetic energy
TUM-AER   = The Institute of Aerodynamics (AER) of the Technical University Munich (TUM)
WTT   = Wind Tunnel Test

I. Introduction

Flow separation from smooth surfaces continues to dominate the configuration aerodynamics of many flight vehicles. In many cases, such flows are unavoidable. One example are configurations with highly swept wings and blunt leading-edges, such as supersonic business jets at low-speed flight conditions and many Uninhabited Combat Air Vehicles (UCAV's) during maneuver where leading edge vortex flows dominate the stability and control characteristics. Another example is the new hybrid wing-body concept under consideration for next-generation civil transports where the avoidance of forebody vortex ingestion into the aft-mounted upper surface engines becomes a crucial design criteria. For each case, the accurate prediction of moderately swept blunt leading-edge separation is critical to mitigating the risks in the final design. The shortcomings of such predictions stem from continued deficiencies in our models of transition and turbulence. This challenge is being addressed by an international body of researchers under the NATO/STO AVT-183 Task Group titled "Reliable Prediction of Separated Flow Onset and Progression for Air and Sea Vehicles".

The AVT-183 task group is focusing on the swept blunt leading-edge flow separation problem using a 53^0 swept diamond wing [1]. The particular geometry was devised as a simplified unit problem of the leading edge region of the 53^0 swept Stability and Control Configuration (SACCON) configuration studied by the NATO/STO AVT-161 Task Group titled "Assessment of Stability and Control Prediction Methods for NATO Air & Sea Vehicles" [2]. The objective of AVT-183 is to conduct a new series of wind-tunnel experiments to gather a unique and comprehensive experimental aerodynamic data set for realistic configurations, including: pressures, off-surface velocities, turbulence quantities, etc. to be used to assess, diagnose and improve the current state-of-the-art CFD methods for predicting the onset and progression of flow separation, and associated unsteady phenomena. Significant input was solicited from turbulence model experts during the design of the AVT-183 experimental campaign. A thorough overview of this effort is presented in Ref. [1].

The challenges facing the computational aerodynamicist is illustrated in Figure 1 where five distinct flow types are identified for a blunt leading-edge swept wing that must be modeled simultaneously; 1) the incipient separation that coalesces into 2) the leading edge vortex that induces 3) the secondary vortex separations, that are bracketed by 4) the inner attached flow and 5) an inner vortex separation. This presents a formidable challenge for CFD prediction tools.

The objective of the current study is to augment the AVT-183 experimental campaign with additional insights derived from the computed diamond wing flow field that might enable turbulence experts to further improve their models for predicting swept blunt leading-edge flow separation. The organization is as follows. After the preliminary overview of the geometry, experimental data, and methodology, the features of the global flow field will be discussed. This is followed by an analysis of the surface flow characteristics with particular focus on the nature of incipient separation. Finally, details of the off-body vortical flow relevant to turbulence model performance will be examined.

II. Geometry and Experiment

The focus geometry is a simple diamond wing planform [3] shown in Fig. 2 mounted on a metrically isolated peniche to a turntable in the floor of the low-speed wind tunnel at the Institute of Aerodynamics (AER) of the Technical University Munich (TUM). The leading- and trailing edge sweeps are 53° and -26.5^o, respectively. The airfoil section is maintained with a constant NACA 64A006 profile. The peniche standoff distance is $0.075c_R$, where the root chord is c_R=1.2m. Measurements included six components of forces and moments, static surface pressures, unsteady surface pressures, and off-body flow measurements of velocity and velocity fluctuations using hot-wire anemometry (HWA) and particle image velocimetry (PIV) [4,5], of which only the static surface pressure and PIV measurements were available for the present analysis. The wind tunnel model (Fig. 2) was designed as large as practical for measuring flow field velocities in the TUM-AER low-speed tunnel with the HWA/PIV techniques. The test was conducted in an open test section at M_∞=0.15 and Reynolds number Re_{mac}=2.7 million based on mac=2/3*c_R=0.8m.

III.   Methodology

The CFD computations are performed using the NASA Tetrahedral Unstructured Software System (TetrUSS) [6]. This system consists of loosely integrated, user-friendly software that comprises a geometry setup utility GridTool, a tetrahedral grid generator VGRID, a flow solver USM3D, and post-processing visualization and data extraction utilities.

A. Grid generator

VGRID [7,8] is a tetrahedral grid generator based on the advancing front method (AFM) for generation of surface triangles and "inviscid" field cells, and the advancing layers method (ALM) for generation of thin-layered "viscous" cells. Both techniques are based on marching processes in which tetrahedral cells grow from an initial front (triangular surface mesh) until the volume around the geometry is filled. Unlike the conventional AFM, which introduces cells into the field in a totally unstructured manner, the ALM generates organized layers of thin tetrahedral cells, one layer at a time, while maintaining the flexibility of AFM. Once the advancing front process is completed in VGRID, an additional postprocessing step is required using POSTGRID to close any open pockets and to improve grid quality. VGRID input files are generated by an interactive geometry manipulation program, GridTool. This graphics tool can import surface definitions from initial graphics exchange specification (IGES) files containing nonuniform rational B-spline surfaces and curves, as well as PLOT3D point definition files. GridTool is used to manipulate the geometry and to define necessary geometric surface patches and grid spacing (source) parameters.

B. Flow solver

The computations are performed with USM3D [9], which is a parallelized tetrahedral cell-centered, finite volume Navier-Stokes flow solver. The term "cell centered" means that the finite volume flow solution is solved at the centroid of each tetrahedral cell. Inviscid flux quantities are computed across each tetrahedral cell face using various upwind schemes. Spatial discretization is accomplished by a novel reconstruction process, based on an analytical formulation for computing solution gradients within tetrahedral cells. The solution can be advanced in time by a 2nd-order "physical" time step scheme, a 2nd-order "dual" time step scheme, or to a steady-state condition by an implicit backward-Euler scheme. Several turbulence models are available: the Spalart-Allmaras (SA) one-equation model, the two-equation k-ε turbulence model, the Menter Shear Stress Transport (SST) two-equation model, and the nonlinear Algebraic Reynolds Stress Models of Girimaji and Shih/Zhu/Lumley. Detached Eddy Simulation (DES) has been implemented in all of the turbulence models, but has not been fully tested. The latest extensions to the USM3D flow solver are described in Ref. [10].

IV.   Grid Generation

A tetrahedral grid was generated to discretize the domain around the diamond wing/peniche mounted to the wind tunnel floor with free air outer boundaries as shown in Fig. 3. As previously noted, the TUM-AER wind tunnel experiment was conducted in an open test section to facilitate the PIV flow measurements. A thin-layer tetrahedral grid was generated on the wing, peniche, and floor plane to meet requirements for cell-centered computations from the USM3D flow solver. A near-wall first-cell spacing was prescribed, based on flat-plate turbulent boundary layer theory, to achieve a tetrahedral cell centroid turbulent wall coordinate (y^+) of 0.5 at a longitudinal distance of $0.5*mac$ for a Re_{mac}=2.7 million. Since the VGRID Advancing Layers Method marches nodes away from the vertices of the surface triangles (which are subsequently connected to form tetrahedral cells), an initial VGRID spacing, δ_1, corresponding to a $y^+=2$ at the first node was prescribed in order to achieve the $y^+=0.5$ at the first cell centroid. Subsequent USM3D computations confirmed that an average first-cell $y^+\approx0.5$ was achieved. The nominal wind tunnel chord Reynolds number of 2.7 million required VGRID first-node spacing is $\delta_1/mac=1.775E-05$, and stretching factors of $rate1=0.15$ and $rate2=0.02$, where the nodal spacing layers are defined by the Eq. (1).

$$\delta_{i+1}= \delta_1 \cdot [1+ rate1 \cdot (1+ rate2)^i]^i \tag{1}$$

This "viscous" spacing distribution results in approximately 72 tetrahedral cells (24 nodes) across the boundary layer at the mid-chord of mac.

The surface triangulation on the wing/peniche is shown in Fig. 4. It was necessary to truncate the sharp trailing edge of the NACA 64A006 airfoil at the 99% chord station to create a small blunt edge to facilitate grid generation. As observed in Fig. 4, grid clustering was applied in regions of expected strong gradients, such as the leading and trailing edges, under the vortex, and along the peniche/floor juncture. A visual rendition of the volume grid is

presented in Fig. 5 using cuts of the tetrahedra at various stations. The lower right image in Fig. 5 highlights the triangular face-centered resolution around the leading edge where a 5-to-1 stretching is applied along the leading edge. There the triangle spacing is 0.32mm around the leading edge, and 1.60mm along the edge.

The final grid resolves the domain with 17,975,445 tetrahedral cells (2,948,276 nodes). The surface of the wing is resolved with 150,115 triangle faces, the peniche with 37,872 faces, and the tunnel floor with 18,703 faces.

V. Results and Discussion

The AVT-183 diamond wing was designed to yield a vortex separation midway along the blunt leading edge at around $\alpha=12^o$ [3]. Measurements were obtained during the TUM-AER experiments [4,5] in 1-degree increments in angle of attack from $\alpha=10^o$ to 15°. Since the focus of the present paper is on the incipient leading-edge separation, the majority of analysis will be presented at the $\alpha=12^o$ condition. The additional angles of attack will only be referenced briefly. Only a subset of the TUM-AER data that included surface pressure and off-body vorticity was available during this analysis and is used in the following discussions.

The numerical results are generated by the Reynolds Averaged Navier-Stokes (RANS) formulation using the standard SA [11] and SST [12] turbulence models[2]. All solutions are advanced with 2nd order "physical" time stepping with 9 inner iterations using a characteristic time step of $\Delta t^*=\Delta t \cdot U_\infty/mac$ =0.02 for 1170 steps. Convergence of forces and moments to steady state was verified. Spatial discretization is accomplished using 2nd order upwind Roe's Flux Difference Splitting without flux limiters.

The following analysis will begin with a global characterization of the diamond wing flow field. This is followed by an analysis of the surface flow characteristics with particular focus on the region of incipient separation. Finally, causative quantities produced by the turbulence models in the off-body vortical flow will be examined.

A. Characterization of the flow field

A global features of the diamond wing flow field at $\alpha=12^o$ are conveyed in Fig. 6 through the qualitative correlations of off-body and surface flow parameters from the experimental (upper image) and computational (lower image) data. The experimental image contains the PIV-measured vorticity contours at stations x/c_R=0.1, 0.2, 0.295, 0.395, 0.5, and 0.6, where root chord c_R=1.2m. The USM3D/SA solution in the lower image portrays the fractional total pressure loss (P_T loss) at the same stations, in addition to surface velocity traces colored by pressure coefficient C_p, and a trace of the vortex core. From this correlation, the location and size of the part-span leading edge vortex is qualitatively similar between experiment and computation. As will be shown in subsequent analysis, the SST model initiates the incipient vortex separation further forward on the leading edge making such direct correlation difficult. Hence this fortunate correlation with the USM3D/SA result will be useful for inferring details within the experimental flow field.

In the USM3D/SA solution in Fig. 6, the vortex is observed emerging from a region midway along blunt leading edge and continuing down stream over the outer portion of the wing. The clustering of the vortex reattachment line is evident inboard of the vortex. In the aft wing region, the trace of the vortex core displays some instability, which along with the associated diffusion of the reattachment line may indicate vortex breakdown. A second clustering of converging streamlines is observed in the predominately attached flow region of the wing where an "inner" vortex is forming. Also note that the tunnel floor boundary layer is confined to the peniche, and the flow onto the wing just outboard of the peniche appears reasonably undisturbed and well behaved. The thickness of the incoming floor boundary layer in the computational solution was assessed to affect approximately 40mm, or 44% of the 90mm peniche. The estimates by the TUM-AER experimentalists was approximately 50mm, or 55% of the peniche.

B. Analysis of surface flow
1. Overall surface characteristics

The analysis continues in Figure 7 with a closer examination of the streamtraces[3] that are superimposed onto the surface pressure contours of the USM3D/SA and /SST solutions at $\alpha=12^o$. The previous station cut locations are indicated for reference. The footprint of the leading edge vortex is clearly evident from the C_p contours and streamtraces, as is the large region of developing incipient separation. This figure clearly shows the SST model initiating incipient separation and subsequent leading edge vortex formation further forward along the leading edge

---

[2] NASA Langley Research Center, Turbulence Modeling Resource: http://turbmodels.larc.nasa.gov/
[3] The streamtraces are constructed by applying the averaged velocities at the first nodes off of the surface where $y^+\approx 2$ to the surface nodes.

than that from the SA model. The SA model also produces secondary vortex separation along the leading edge, whereas the SST model does not. The latter may be indicative of a grid that is too coarse in that region. The presence of the inner wing vortex is also evident in both solutions from the converging streamtraces caused by the reattached vortex flow competing with the inner wing attached flow. No discernable pressure footprint is observed within the resolution of the C_p contours indicating, as expected, that its strength is much less than that of the leading edge vortex.

Also plotted along the leading edge of the planforms in Figure 7 is the $C_{p,LE}$ distribution at z=0. The $C_{p,LE}$ decreases almost linearly along the leading edge until a critical level of minimum $C_{p,LE}$ is reached near the origin of the leading-edge vortex. From that point on, the $C_{p,LE}$ returns to more positive values indicating a loss of leading edge suction force which, consistent with the Polhamus suction analogy [13], is recovered in the upper surface vortex suction force. Interestingly, an extrapolation of the converging streamtraces for the inner vortex intersects the leading edge slightly ahead of the point of minimum $C_{p,LE}$.

The spanwise C_p distributions for $\alpha=12^o$ at the six chord stations is shown in Figure 8 comparing the SA and SST results with the TUM-AER data. The USM3D/SA pressure coefficients correlate very well with the experimental measurements, thereby lending credence to the assumption that this computational flow result may be representative of the experimental flow field inferred in Figure 6. This is a fortunate result since the C_p correlations at the other angles of attack between $\alpha=10^o$ and 15° included in the Appendix show no clear winner, with the possible exception of $\alpha=13^o$.

The analysis returns to the $C_{p,LE}$ distributions in Figure 9, replotted from Figure 7 for direct assessment of turbulence model effects. An accompanying comparison with skin friction coefficient $C_{f,LE}$ along z=0 is included as well. In general, both turbulence models produce near identical levels of $C_{p,LE}$ and $C_{f,LE}$ prior to their critical peak locations. But the SST model induces earlier separation at a less negative value of $C_{p,LE}$ than the SA model. Since leading-edge separation for this class of untwisted blunt leading-edge swept wing with constant airfoil section begins at the wing tip and progresses forward with increasing angle of attack, then the onset of incipient separation at a particular angle of attack is most likely modulated by mechanisms within the turbulence models that sensitize the flow to strong pressure gradients.

2. Analysis of incipient separation

Attention is now turned to the region of incipient separation that culminates with the formation of a part-span leading-edge vortex. Figures 10 and 11 illustrate some cursory observations within this region for the USM3D/SA, $\alpha=12^o$ solution, some of which are quantified in Table 1. The region of incipient separation is defined by a set of dividing streamtraces that cross the leading edge at $x/c_R=0.166$, z=0 (see Table 1, SA) where the force balance between streamwise inertia and spanwise pressure gradients is tipped. All boundary layer flow downstream of $x/c_R=0.166$ is contained outboard of these dividing streamtraces and eventually returns to the leading edge. All streamtraces upstream of $x/c_R=0.166$ continue across the predominately attached flow wing upper surface and exits at the trailing edge. A secondary dividing streamtrace also exists between the station of minimum $C_{p,LE}$ and the minimum C_p under the vortex where all flow ahead of this line continues into the secondary vortex system along the leading edge, and all flow aft of this line becomes entrained into the primary vortex system. In Figure 10, white dotted lines are used to trace the minimum pressure trough under the vortex and to extrapolate the vortex reattachment line to the leading edge. These lines intersect at the leading edge slightly upstream of minimum $C_{p,LE}$ as did the extrapolation of the inner vortex streamtraces in Figure 7.

The anatomy of the incipient separation is further exemplified in Figure 11 by the coalescence of attached flow around the leading edge into converging streamtraces that form into a distinct line of separation near $x/c_R=0.285$ (Table 1, SA). This line represents the initial formation of a feeding shear layer that serves to organize the boundary layer vorticity into the initial stages of a vortex core. This feeding sheet continues to strengthen the core until it leaves the surface as a well organized free vortex near the point of $C_{p,LE}=-6.99$ at $x/c_R=0.321$. The minimum $C_p=-3.93$ under the primary vortex occurs slightly further downstream at $x/c_R=0.378$, which corresponds to the inflection of the coalesced streamtraces between the region of incipient separation and the vortex reattachment line, after which the vortex footprint expands downstream with an accompanying increase in surface pressure. These details are also present in the USM3D/SST solution, although the positions are different as noted in Table 1. But the question still remains about what mechanisms within the turbulence models produce these differences.

Table 1. Position of key flow features on 53^0 swept diamond wing. α=12 deg, M$_\infty$=0.15, Re$_{mac}$=2.7x10^6.

USM3D	Flow Property	x/c_R	X, mm	Y, mm	Z, mm	Cp
SA	Dividing ST's around LE	0.166	198.93	149.90	0.00	--
	Converging ST's	0.285	342.54	252.29	5.04	--
	Min C$_{p,LE}$ on round LE	0.321	385.20	290.15	0.74	-6.99
	Min C$_p$ under vortex	0.378	453.92	323.10	7.81	-3.93
SST	Dividing ST's around LE	0.119	143.31	107.99	0.00	--
	Converging ST's	0.203	243.73	178.64	5.15	--
	Min C$_{p,LE}$ on round LE	0.213	256.39	192.91	1.31	-5.09
	Min C$_p$ under vortex	0.269	322.22	223.42	9.08	-3.35
	Max TKE in vortex core (0.22)	0.311	373.62	251.73	17.00	--

C. Analysis of off-body flow

The analysis continues with an examination of the off-body flow field. The role of a turbulence model is to construct a simplified representation the Reynolds stress term in the RANS equations that mimics the effect of momentum transfer from turbulence. The common output from standard turbulence models is an additional component of turbulent viscosity, which modulates the viscous dissipation in the flow. For most models, turbulent production is generated from either vorticity or strain rate. Both the SA and SST results in this study use vorticity in the turbulent production term. The following discussion will first establish correlations of the off-body vorticity between the computational solutions and experimental measurements. Then the relationships between the underlying turbulent viscosity and SST turbulent kinetic energy (TKE) are examined. And finally, a more extensive examination of the SST model TKE is presented.

Figure 12 portrays off-body normalized x-vorticity contours at the six chord stations at α=12° for the TUM-AER experiment and the SA and SST turbulence models. The contour scales of the normalized vorticity have been clipped at $\pm$50 with color removed around zero to increase clarity. As noted in Figure 6, close similarities in leading-edge vortex position and size are observed between the TUM-AER PIV data and USM3D/SA solution. The initial vortex formation in USM3D/SST solution is further forward as noted previously. While the vorticity contour levels are remarkably similar, their levels in the TUM-AER data appear slightly lower in the attached-flow and core regions compared to the USM3D/SA result.

Corresponding off-body contours of computed turbulent viscosity and TKE are shown in Figure 13, which as expected increase in level toward the vortex core since turbulent production is driven by vorticity. The presence of the inner vortex is also evident. Inset in the upper right are representative profiles of turbulent viscosity and TKE through the vortex along a vertical line extending from a common reference point of minimum surface C$_p$ under the vortex (see Table 1, Figures 10 and 11). Note that the maximum level of turbulent viscosity for the SA model is approaching twice that of the SST model. However, the turbulent viscosity levels of the SST model are higher near the surface than for the SA model; a property that may have relevance to the differing locations of incipient separation. This plot also provides direct correlation between profiles and levels of turbulent viscosity and the TKE in the SST solution.

Figure 14 presents a ¾-view of the off-body TKE contours relative to the key surface flow features noted in previous analysis and in Table 1 (SST). The TKE contours are plotted on a plane cutting through the vortex core and through the five x/c_R stations noted for the SST model in Table 1. The second and third contours at the converging streamtraces and minimum C$_{p,LE}$ on round LE respectively show evidence of TKE buildup in the boundary layer of the incipient separation region. Aft of those stations, the TKE buildup becomes entrained into the evolving leading-edge vortex system. An interrogation of the entire flow field yielded a location of maximum TKE, k/U^2_∞=0.22, that occurs in the vortex core at the coordinate recorded in the last entry of Table 1 and noted within the intersecting contours in Figure 14.

This surprising result prompted further examination in Figure 15 where the distribution of k/U^2_∞ is plotted along a line very near to the vortex core location. The buildup of TKE begins near the point where the incipient streamtraces converge slightly upstream of the location of minimum C$_{p,LE}$ near where the extrapolated surface flow features noted in Figures 7 and 10 intersected the leading edge. The TKE increases almost linearly up to the location of minimum Cp under the vortex, after which the slope tapers to the location of maximum TKE, k/U^2_∞=0.22, and subsequently decreases thereafter.

V. Summary

A systematic analysis of incipient separation and subsequent vortex formation from moderately swept blunt leading edges has been presented for a 53^0 swept diamond wing at $M_\infty=0.15$ and $Re_{mac}=2.7$ million. The objective was to extract insights from the experimentally measured and numerically computed flow fields that might enable turbulence experts to further improve their models for predicting swept blunt leading-edge flow separation. Details of vortex formation were inferred from numerical solutions after establishing a good correlation of the global flow field and surface pressure distributions between available wind tunnel measurements and computed flow solutions. From this, significant and sometimes surprising insights into the nature of incipient separation and part-span vortex formation were derived. The following observations were recorded during the preceding analysis of the 53^0 swept diamond wing flow field. Unless stated otherwise, these observations apply to the $\alpha=12^0$ condition.

1. Good qualitative correlations of part-span vortex position and strength were established at $\alpha=12^0$ between the TUM-AER PIV-measured flow field and surface C_p distribution data and a corresponding USM3D/SA solution. This fortunate correlation forms the basis of an approach used thereafter to infer details of the vortex formation within the experimental diamond wing flow field from the computational solution at $\alpha=12^0$ (Figures 6, 8, and 12).

   - Correlations of surface C_p distributions at the other angles of attack of 10^0, 11^0, 13^0, 14^0, and 15^0 included in the Appendix were not as fortunate.

   - The USM3D/SST solution at $\alpha=12^0$ produced incipient separation and vortex formation further forward along the leading edge, and could not be correlated with the TUM-AER data directly. However, the features and characteristics of the flow is similar to those of the USM3D/SA solution (Figures 7, 9, and 12).

2. The region of incipient separation is defined by a set of dividing streamtraces that cross the leading edge at z=0 (Figure 10, Table 1) where the force balance between streamwise inertia and spanwise pressure gradients is tipped. All upper surface boundary layer flow aft of this line returns to the leading edge and becomes entrained into either the primary or secondary vortex systems. All flow ahead of this line remains attached to the wing upper surface and leaves at the trailing edge.

   - A secondary dividing streamtrace also exists between the station of minimum $C_{p,LE}$ and the minimum C_p under the vortex where all flow ahead of this line continues into the secondary vortex system along the leading edge, and all flow aft of this line becomes entrained into the primary vortex system.

   - The dividing streamtraces of incipient separation merge into the vortex reattachment line of the primary vortex.

3. While the exact origin of the leading-edge vortex is difficult to discern, lines drawn through the vortex suction peak, the vortex reattachment line, and the clustered stream traces of the inner vortex all converge at the wing leading edge slightly ahead of the point of critical minimum C_p at z=0. This holds for both SA and SST results. (Figures 7, 10)

4. The $C_{p,LE}$ and $C_{f,LE}$ distributions along the leading edge for the SA and SST solutions is near identical up to their critical peak levels. However, the critical minimum $C_{p,LE}$ for the SST model is more positive and hence further upstream, suggesting that the onset of incipient separation at a particular angle of attack is most likely modulated by mechanisms within the turbulence models that sensitize the flow to strong pressure gradients. (Figure 9)

5. The interaction between the competing reattached vortex flow and the inner wing attached flow results in the formation of a weak "inner" vortex on the wing (Figure 7). There is no discernable footprint from this vortex on the surface C_p contours.

6. The levels of off-body vorticity in the TUM-AER PIV data is slightly lower than those from the USM3D/SA and USM3D/SST solutions (Figure 12). Corresponding off-body contours of computed turbulent viscosity and TKE show an expected increase in level toward the vortex core since turbulent production is driven by vorticity (Figure 13).

7. Profiles of turbulent viscosity and TKE through the vortex were extracted, as shown in Figure 13, along a vertical line extending from a common reference point of minimum surface C_p under the vortex (Table 1, Figures 10 and 11). The maximum level of turbulent viscosity for the SA model approaches twice that of the SST model. However, the turbulent viscosity levels of the SST model are higher near the surface than for the SA model; a property that may have relevance to the differing locations of incipient separation. Direct correlation between profiles and levels of turbulent viscosity and the TKE in the SST solution is provided.

8. There is a buildup of TKE in the boundary layer of the incipient separation region that becomes entrained into the developing leading edge vortex. (Figure 14)

9. The maximum level of TKE in the field occurs in the off-body vortex core downstream of the station of minimum C_p under the vortex. The buildup of TKE within the vortex core begins near the point where the incipient streamtraces converge slightly upstream of the location of minimum $C_{p,LE}$ near where the extrapolated surface flow features noted above in Summary item 3 intersected the leading edge. The TKE increases almost linearly within the vortex core up to the location of minimum C_p under the vortex, after which its slope tapers to the location of maximum TKE, k/U^2_∞=0.22, and subsequently decreases thereafter. (Figures 14, 15)

Appendix

Additional correlations of surface C_p distributions of the AVT-183 53^0 swept diamond wing at angles of attack of 10^0, 11^0, 13^0, 14^0, and 15^0 are included in Figures A-1 through A-5. The flow conditions are M_∞=0.15 and Re_{mac}=2.7 million.

Acknowledgments

References

[1] Luckring, J.M., and Boelens, O.J., "A Reduced-Complexity Investigation of Blunt Leading-Edge Separation Motivated by UCAV Aerodynamics", AIAA Science and Technology Forum and Exposition (SciTech 2015) (submitted for publication).

[2] Cummings, R.M., Schütte, A., "Integrated Computational/Experimental Approach to Unmanned Combat Air Vehicle Stability and Control Estimation", *Journal of Aircraft*, Vol. 49, No. 6, November-December 2012, pp. 1542-1557.

[3] Boelens, O.J., Luckring, J.M., Knoth, F., Hövelmann, A., Breitsamter, C., Malloy, D.J., and Deck, S., "Numerical and Theoretical Considerations for the Design of the AVT-183 Diamond-Wing Experimental Investigations", AIAA Science and Technology Forum and Exposition (SciTech 2015) (submitted for publication).

[4] Hövelmann, A., Knoth, F., and Breitsamter, C., "Leading-Edge Roughness Effects on the Flow Separation Onset of the AVT-183 Diamond Wing," AIAA Science and Technology Forum and Exposition (SciTech 2015) (submitted for publication).

[5] Hövelmann, A., Grawunder, M., and Breitsamter. C., "Experimental Analyses on the Flow Field Characteristics of the AVT-183 Diamond Wing," AIAA Science and Technology Forum and Exposition (SciTech 2015) (submitted for publication).

[6] Frink, N.T., Pirzadeh, S. Z., Parikh, P. C., Pandya, M. J., and Bhat, M. K., "The NASA tetrahedral unstructured software system (TetrUSS)," *The Aeronautical Journal*, Vol. 104, No. 1040, 2000, pp. 491-499.

[7] Pirzadeh, S.Z., "Three-Dimensional Unstructured Viscous Grids by the Advancing Layer Method", AIAA Journal, Vol. 33, No. 1, 1996, pp. 43-49.

[8] Pirzadeh, S.Z., "Advanced Unstructured Grid Generation for Complex Aerodynamic Applications", AIAA Journal, Vol. 48, No. 5, 2010, pp. 904-915.

[9] Frink, N.T., "Tetrahedral Unstructured Navier-Stokes Method for Turbulent Flows", AIAA Journal, Vol. 36, No. 11, 1998, pp. 1975-1982.

[10] Pandya, M.J., Frink, N.T., Abdol-Hamid, K.S., Samareh, J.A., Parlette, E.B., and Taft, J.R., "Enhancements to TetrUSS for NASA Constellation Program," *Journal of Spacecraft and Rockets*, Vol. 49, No. 4, 2012, pp. 617-631.

[11] Spalart, P.R. and Allmaras, S.R., "A One-Equation Turbulence Model for Aerodynamic Flows," *Recherche Aerospatiale*, No. 1, 1994, pp. 5-21.

[12] Menter, F.R., "Two-Equation Eddy-Viscosity Turbulence Models for Engineering Applications," *AIAA Journal*, Vol. 32, No. 8, August 1994, pp. 1598-1605.

[13] Polhamus, E.C., "A Concept of the Vortex Lift of Sharp-Edge Delta Wings Based on a Leading-Edge-Suction Analogy", NASA TN D-3767, 1966.
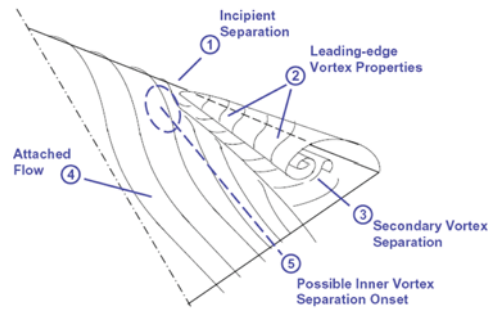
Figure 1. Sketch of diamond wing flow features [1].
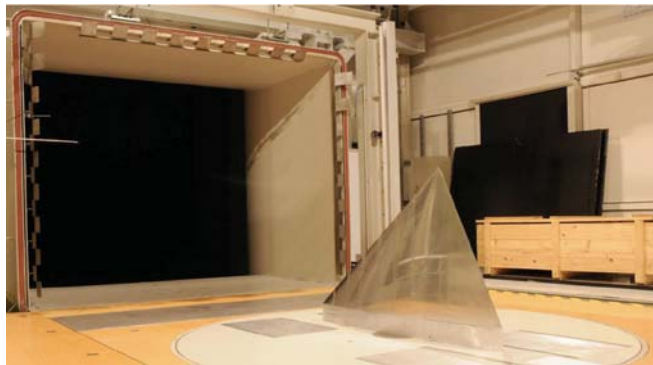
Figure 2. Diamond wing model including peniche mounted on turntable floor of TUM-AER wind tunnel.
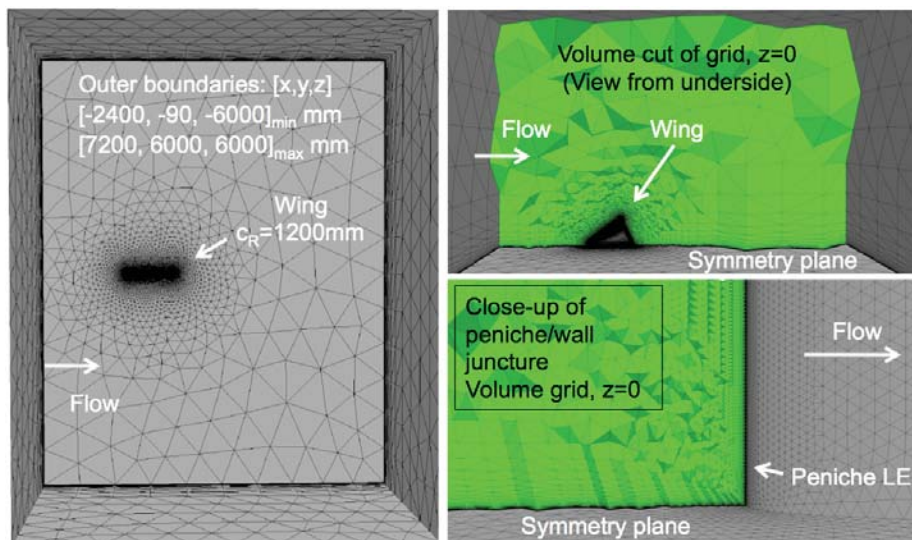
Figure 3. Computational domain (flow from left to right). Left – side view. Right – top view volume grid cut through z=0 plane, bottom view close-up of peniche/wall juncture region.
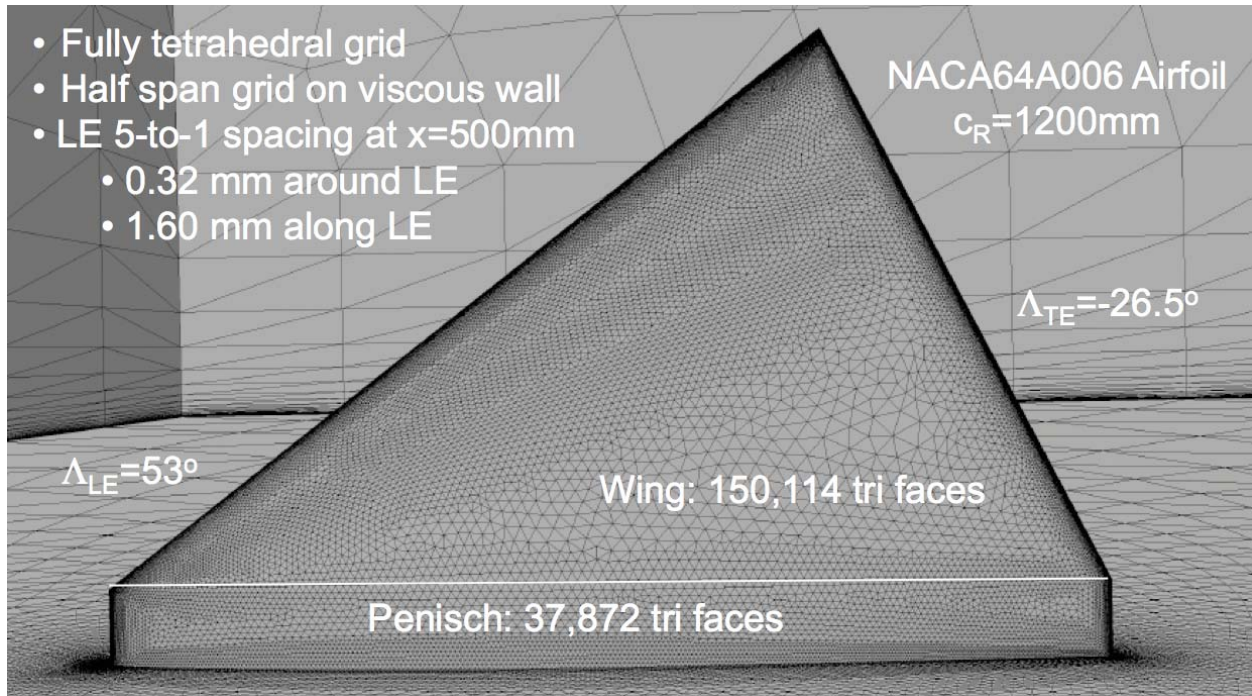
Figure 4. Surface triangulation on diamond wing/peniche.
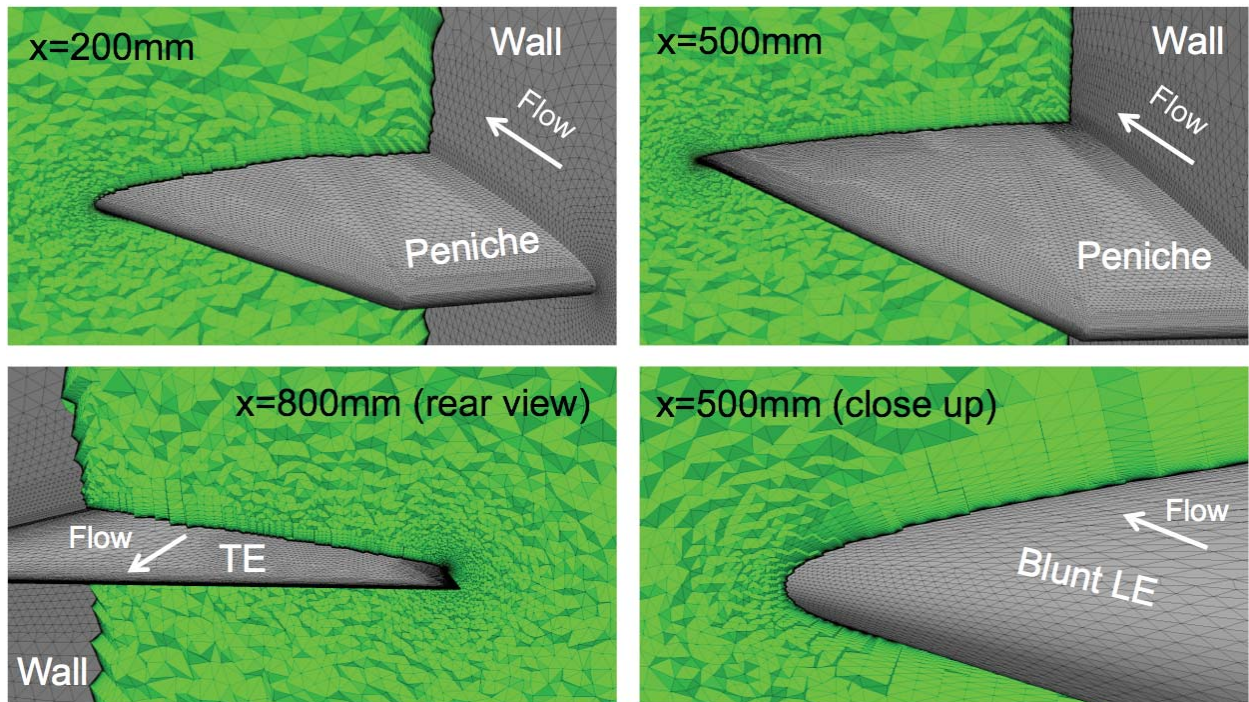
Figure 5. Cut planes of volume grid, with detail around blunt leading edge of diamond wing. Total number of tetrahedral cells 17,319,128.
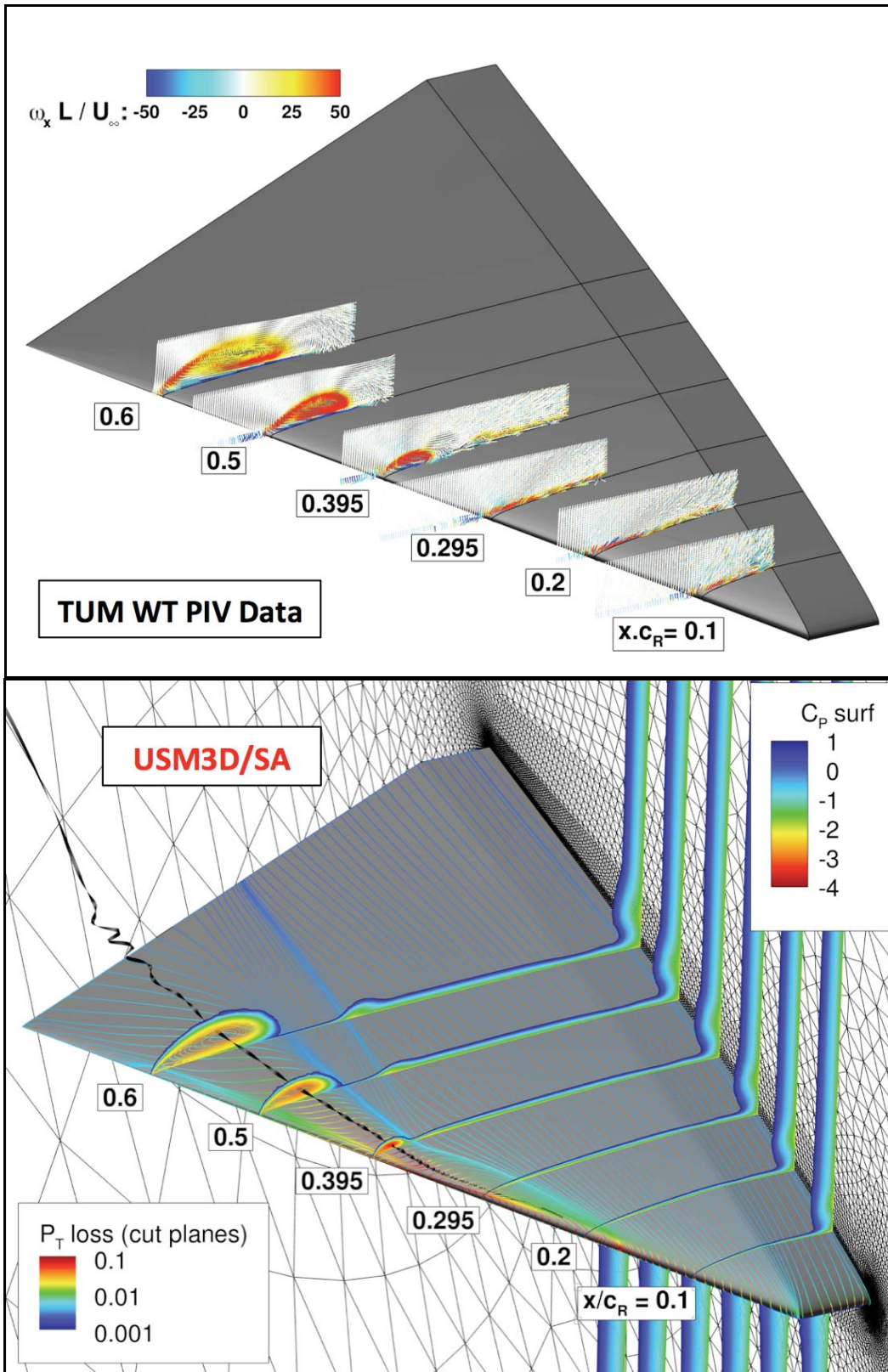
Figure 6. **Global features of 53⁰ swept diamond wing flow field. Top – TUM-AER off-body vorticity. Bottom – USM3D/SA off-body total pressure loss, surface flow and C_p. $\alpha=12^0$, $M_\infty=0.15$, $Re_{mac}=2.7x10^6$.**

American Institute of Aeronautics and Astronautics
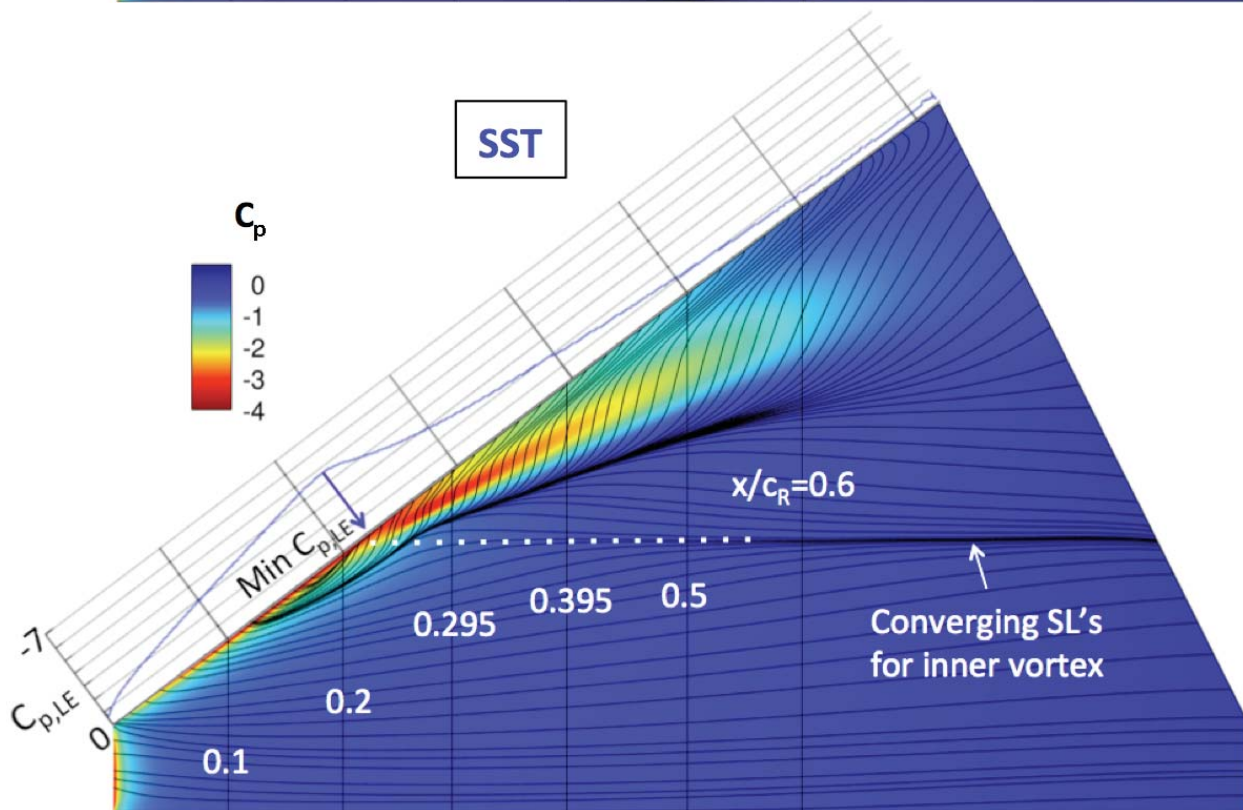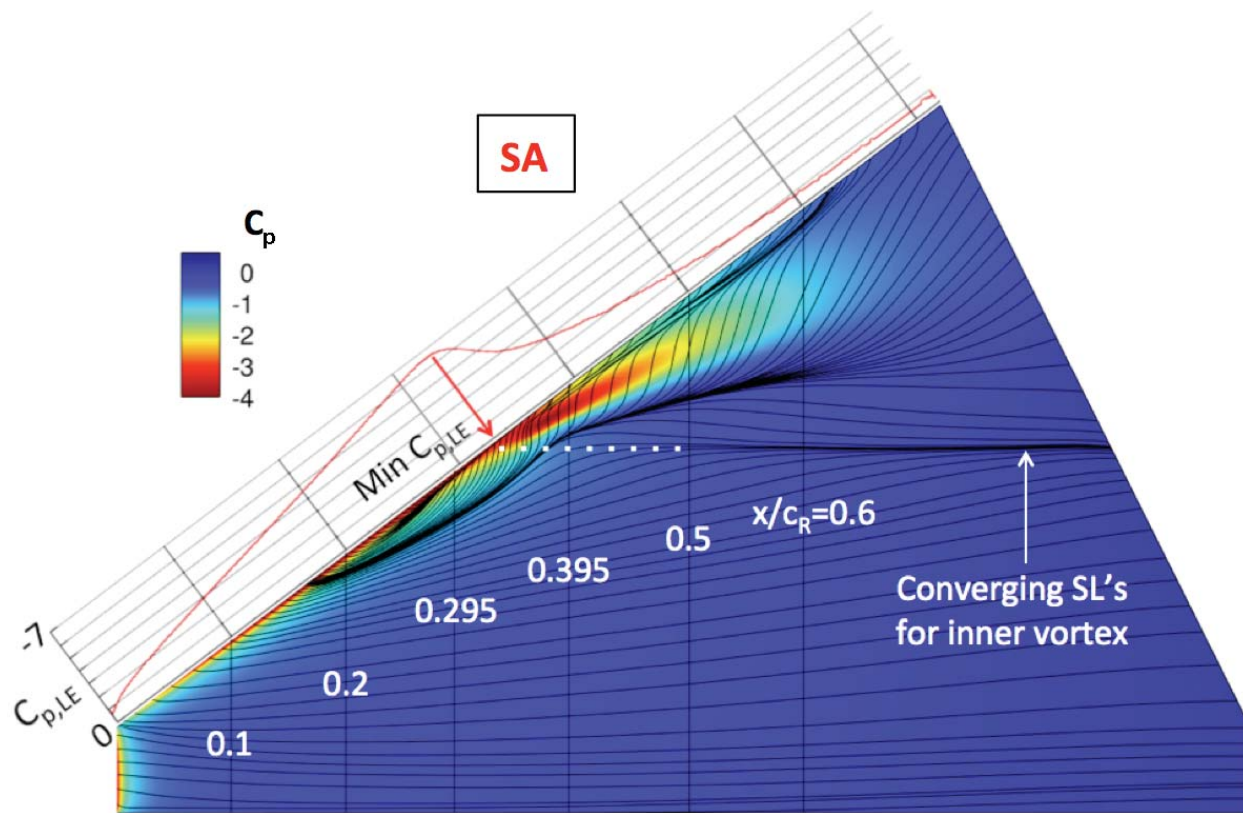
Figure 7. Effect of turbulence model on surface Cp contours and streamtraces. Top - USM3D/SA, Bottom - USM3D/SST. $\alpha=12^0$, $M_\infty=0.15$, $Re_{mac}=2.7\text{x}10^6$.

American Institute of Aeronautics and Astronautics
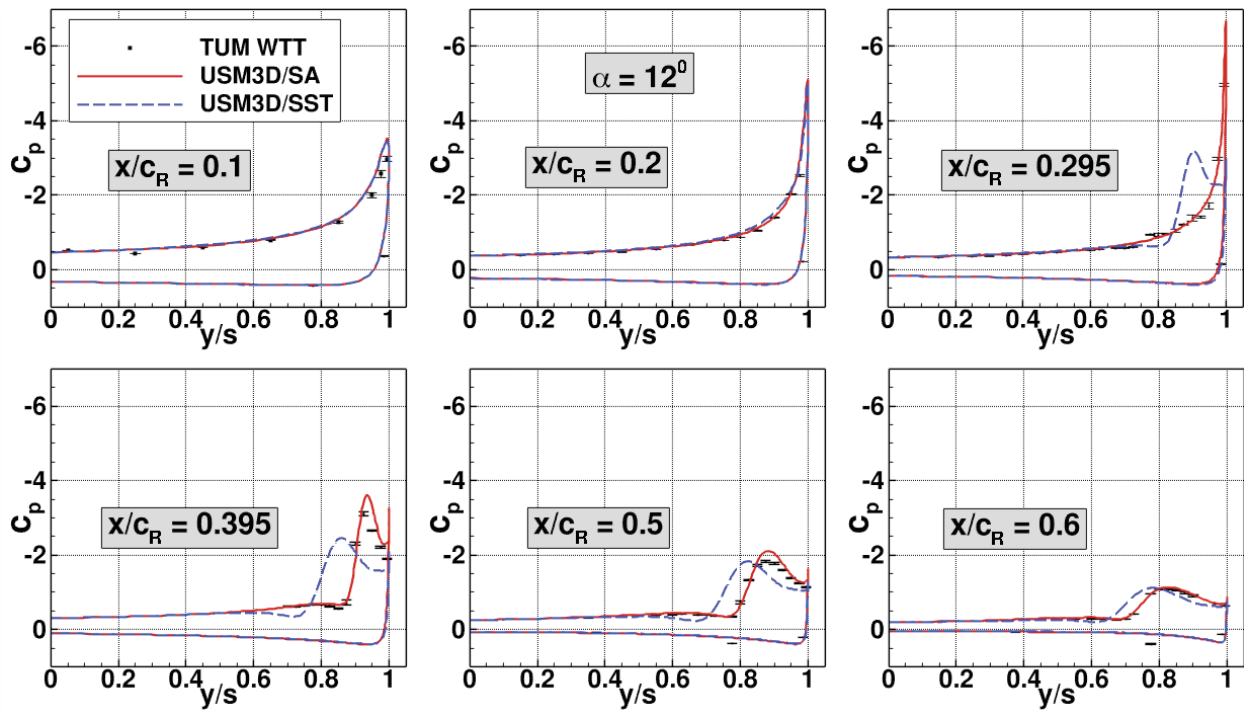
Figure 8. Effect of turbulence models on spanwise C_p distributions. $\alpha=12^0$, $M_\infty=0.15$, $Re_{mac}=2.7\times10^6$.
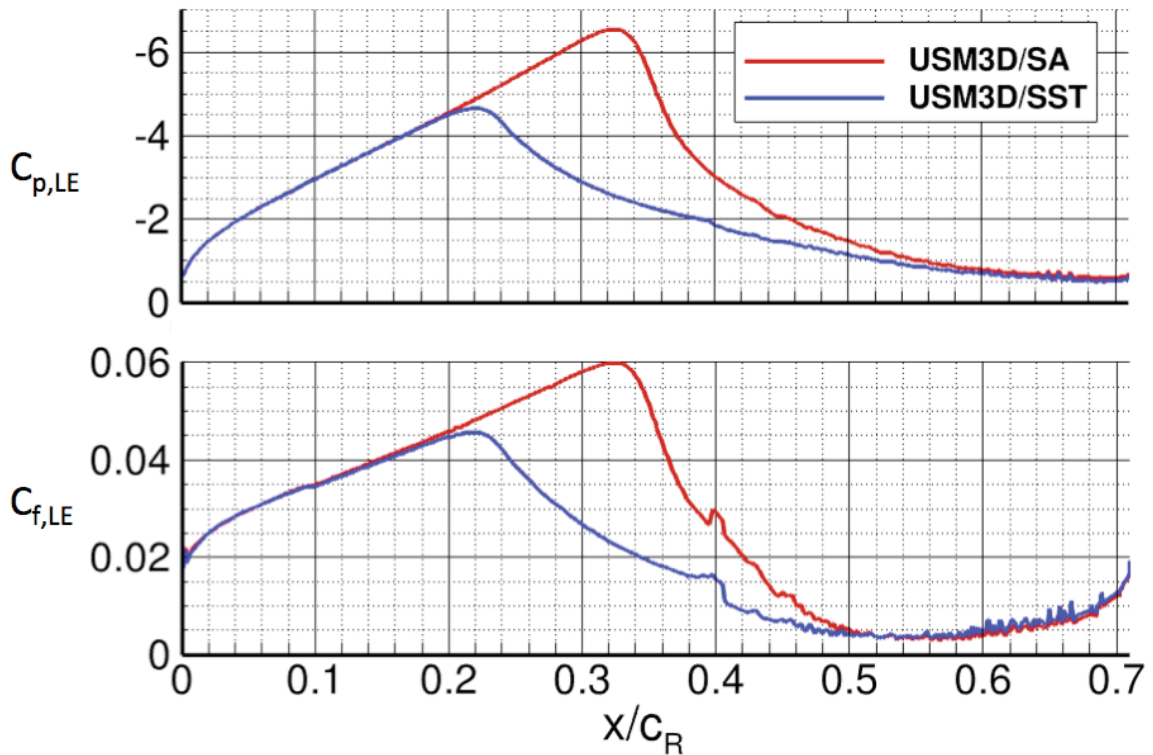
Figure 9. Effect of turbulence model on the distribution of pressure and skin friction coeffiients along the leading edge, z=0. $\alpha=12^0$, $M_\infty=0.15$, $Re_{mac}=2.7\times10^6$.

American Institute of Aeronautics and Astronautics
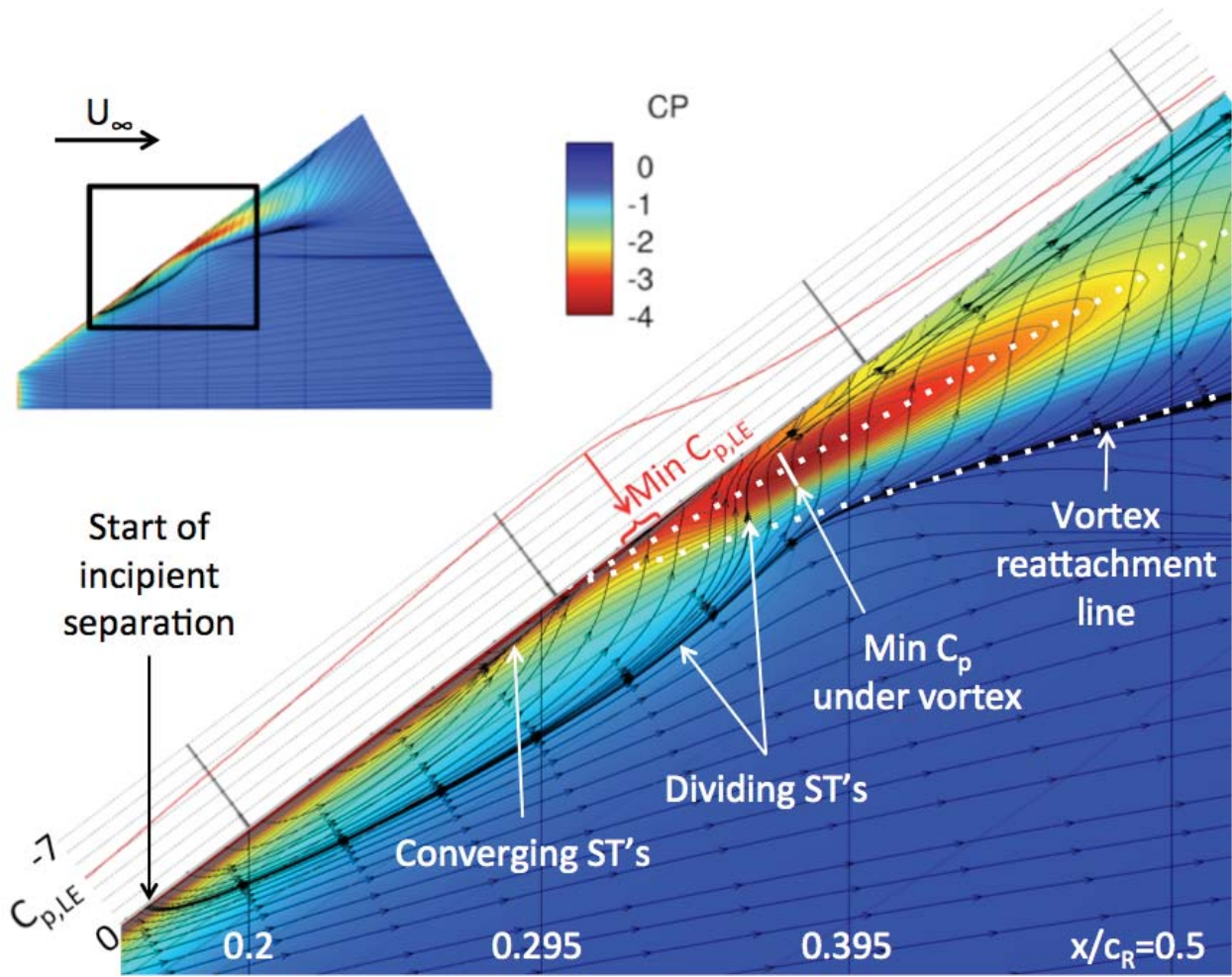
Figure 10. Features of developing incipient separation and leading edge vortex formation. USM3D/SA, $\alpha=12^0$, $M_\infty=0.15$, $Re_{mac}=2.7\times10^6$.
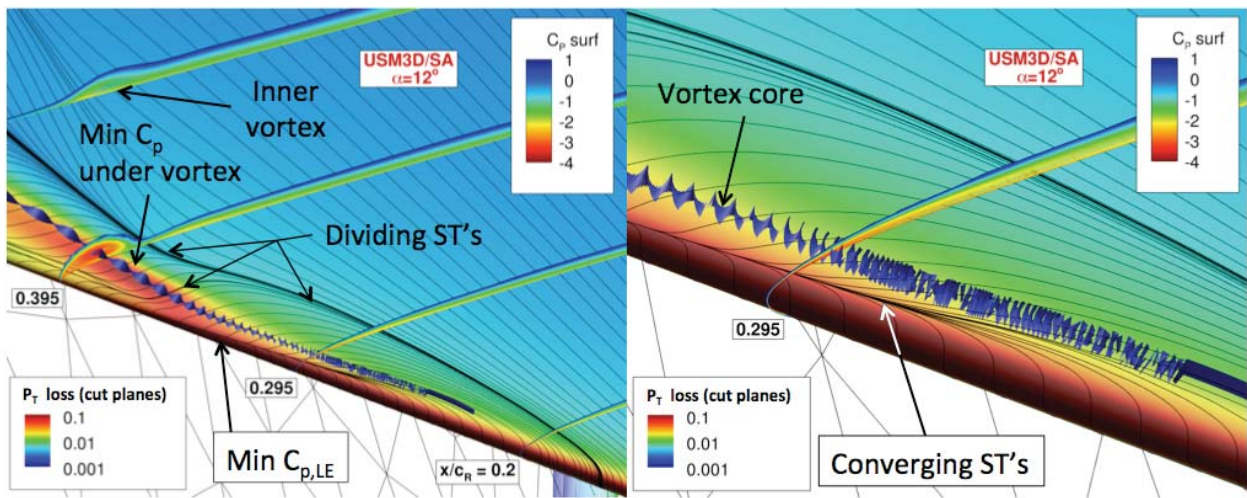
Figure 11. Close-up of incipient separation and initial stage of leading-edge vortex formation. Flow from right to left. USM3D/SA, $\alpha=12^0$, $M_\infty=0.15$, $Re_{mac}=2.7\times10^6$.
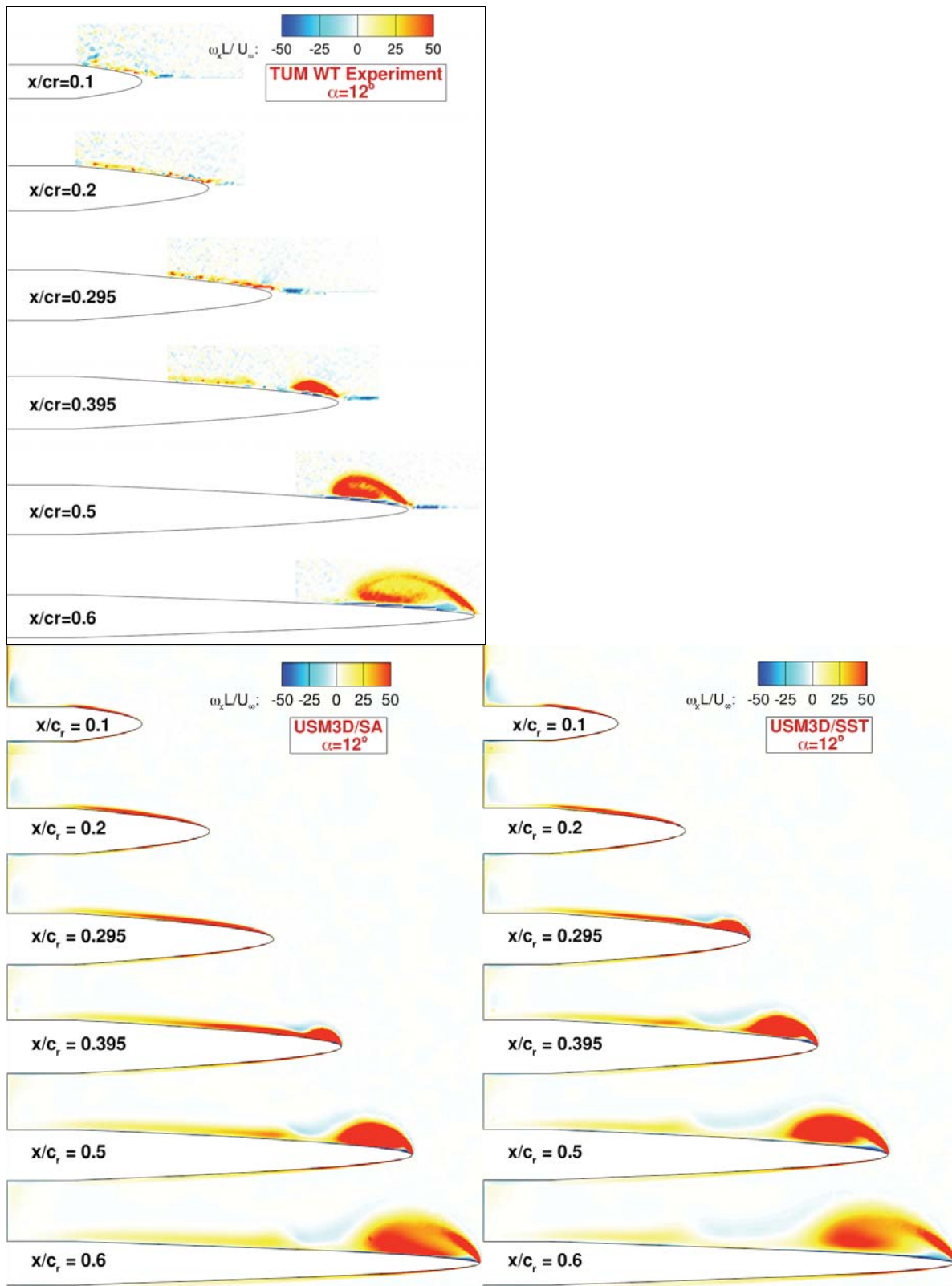
Figure 12. Correlations of experimental and CFD x-vorticity contours at six chord stations. $\alpha=12^0$, $M_\infty=0.15$, $Re_{mac}=2.7x10^6$.

American Institute of Aeronautics and Astronautics
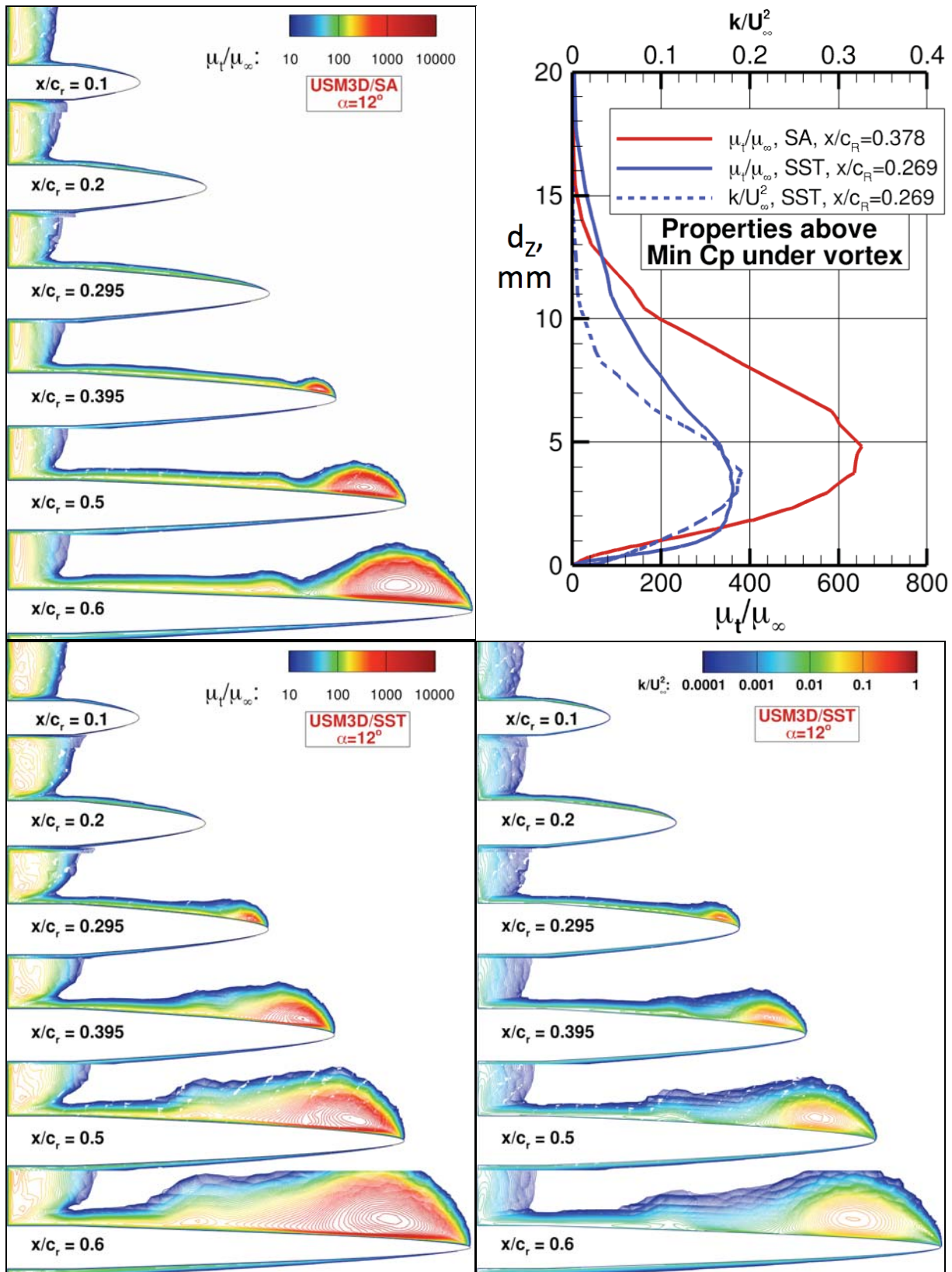
Figure 13. Contours of computed off-body viscosity and turbulent kinetic energy. USM3D/SA and USM3D/SST. $\alpha=12^0$, $M_\infty=0.15$, $Re_{mac}=2.7 \times 10^6$.
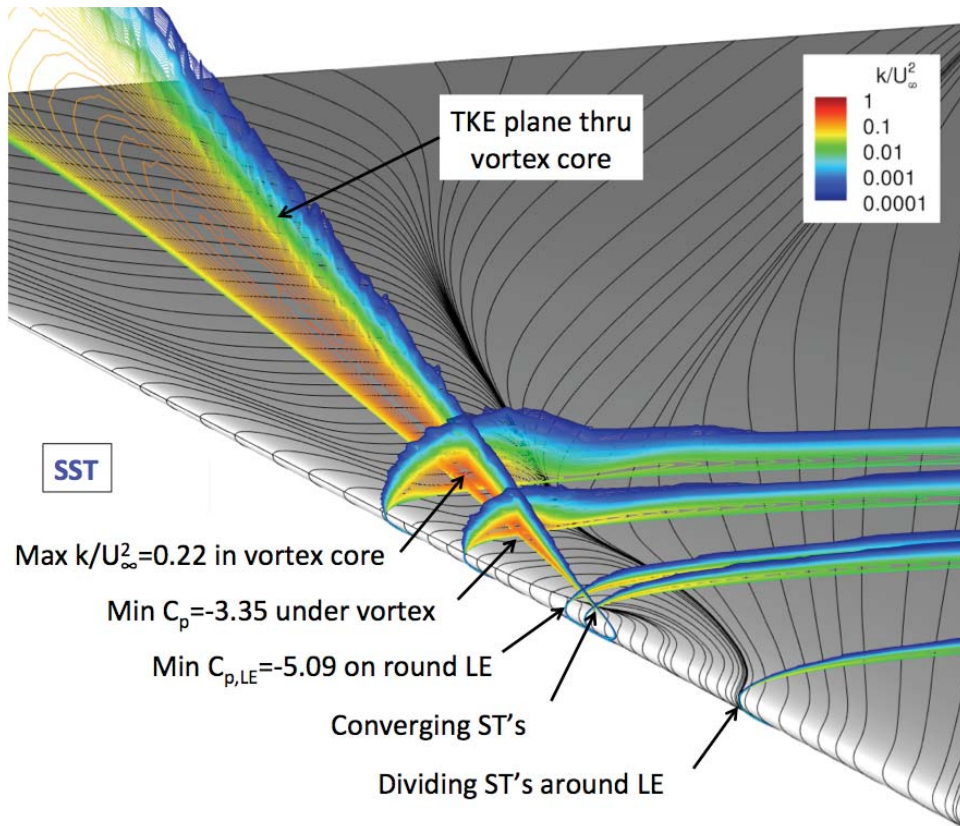
Figure 14. TKE field contours at stations of key USM3D/SST flow features identified in Table 1. $\alpha=12^0$, $M_\infty=0.15$, $Re_{mac}=2.7\text{x}10^6$..
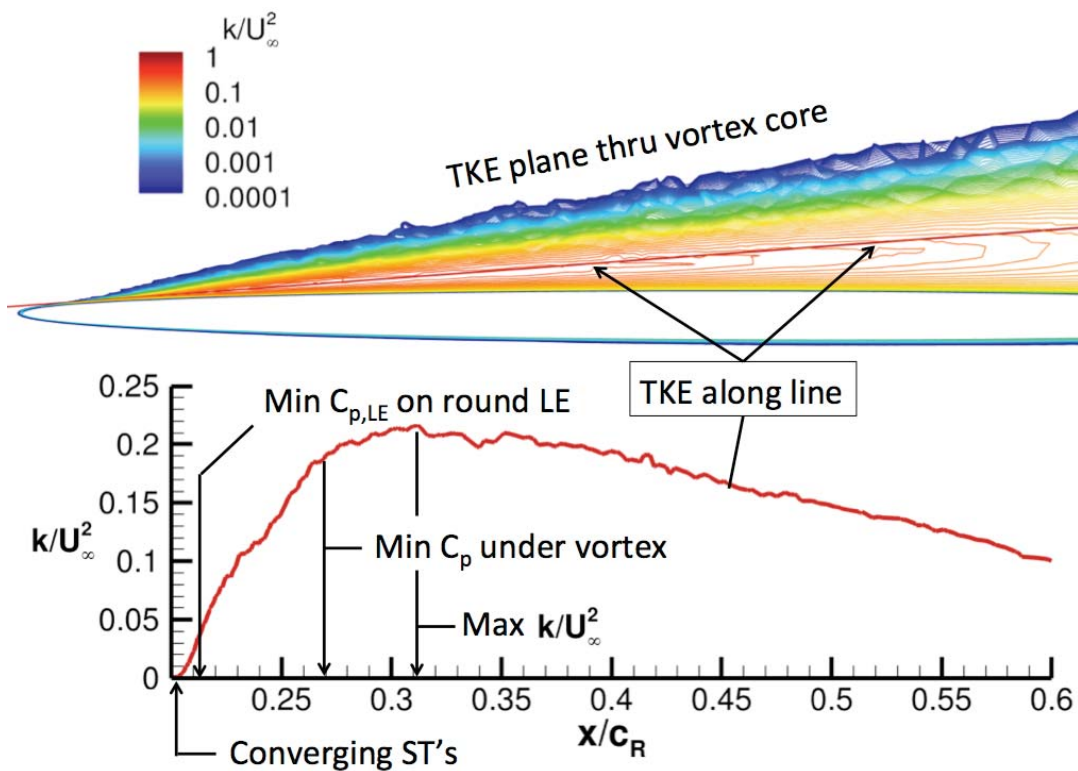
Figure 15. Turbulent kinetic energy profile along vortex core. USM3D/SST. $\alpha=12^0$, $M_\infty=0.15$, $Re_{mac}=2.7\text{x}10^6$.
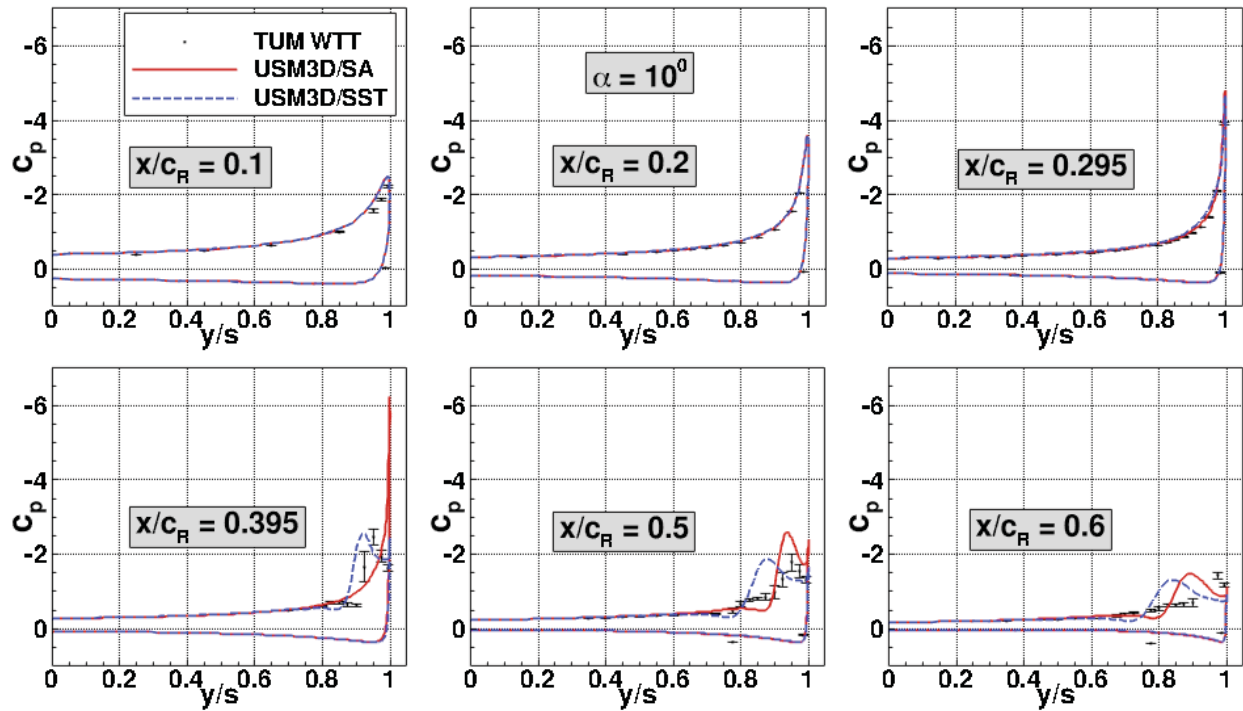
American Institute of Aeronautics and Astronautics

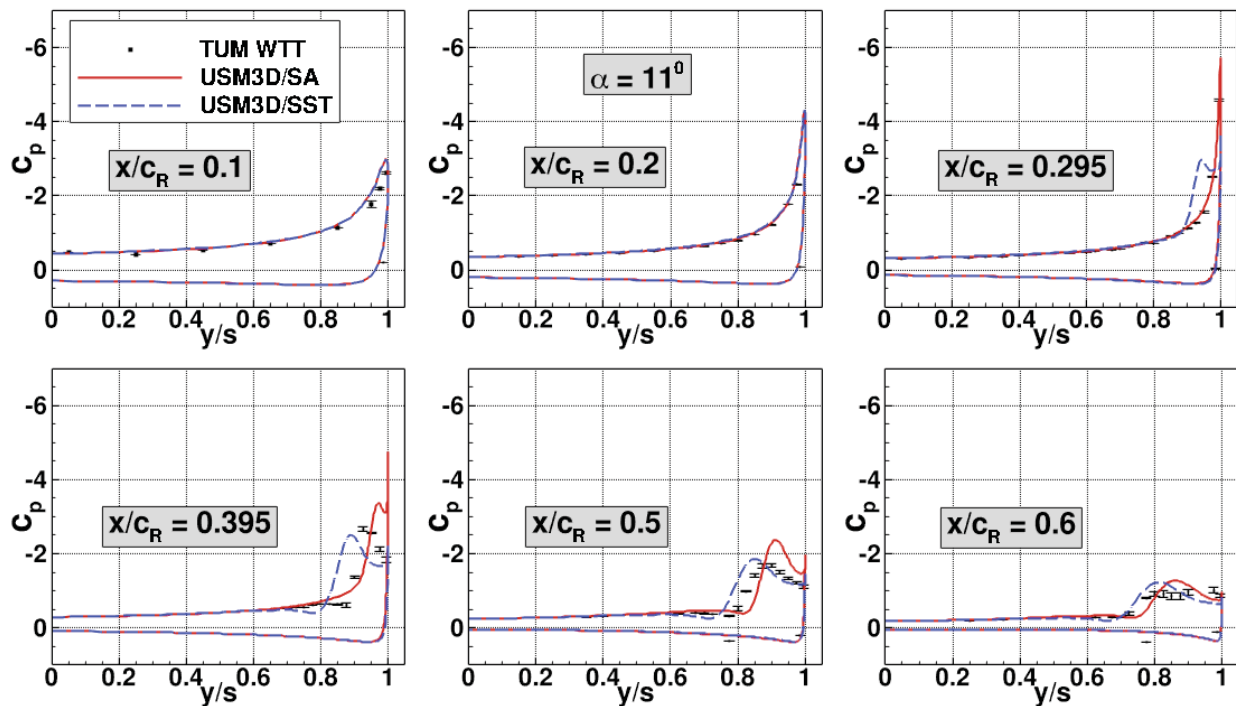**Figure A-1 . Effect of turbulence models on spanwise C_p distributions. $\alpha=10^0$, $M_\infty=0.15$, $Re_{mac}=2.7\times10^6$.**

Figure A-2. Effect of turbulence models on spanwise C_p distributions. $\alpha=11^0$, $M_\infty=0.15$, $Re_{mac}=2.7\times10^6$.
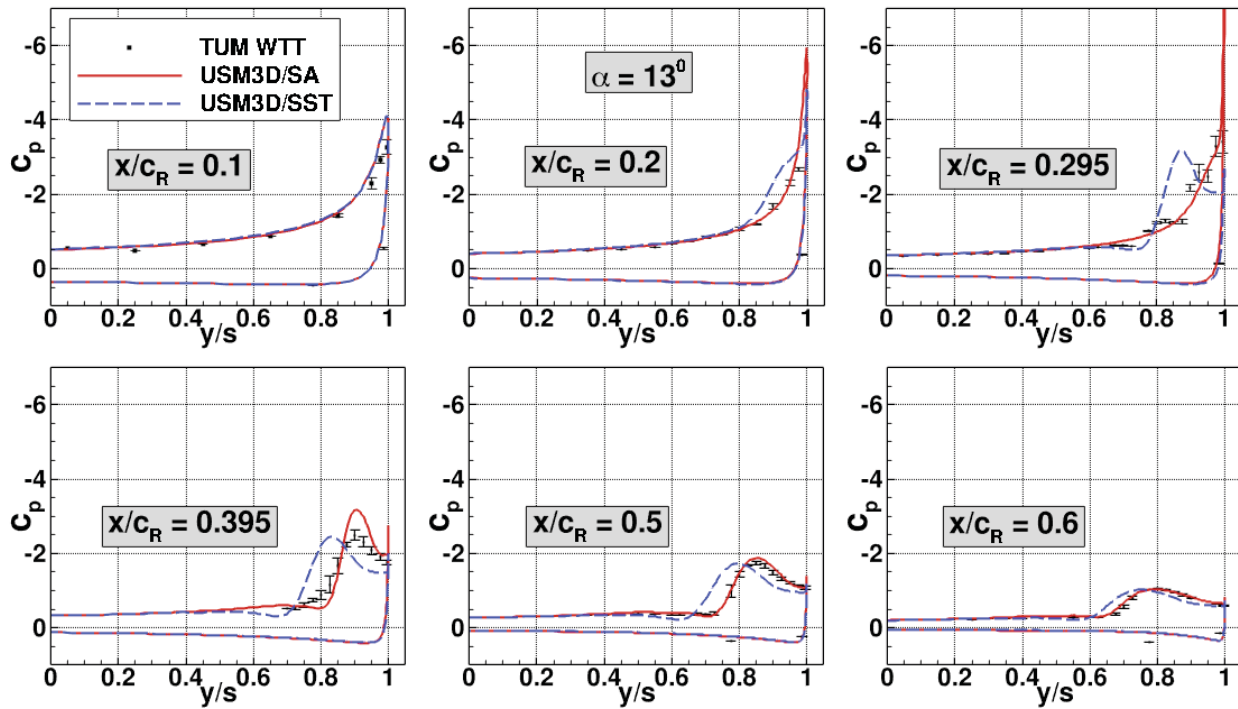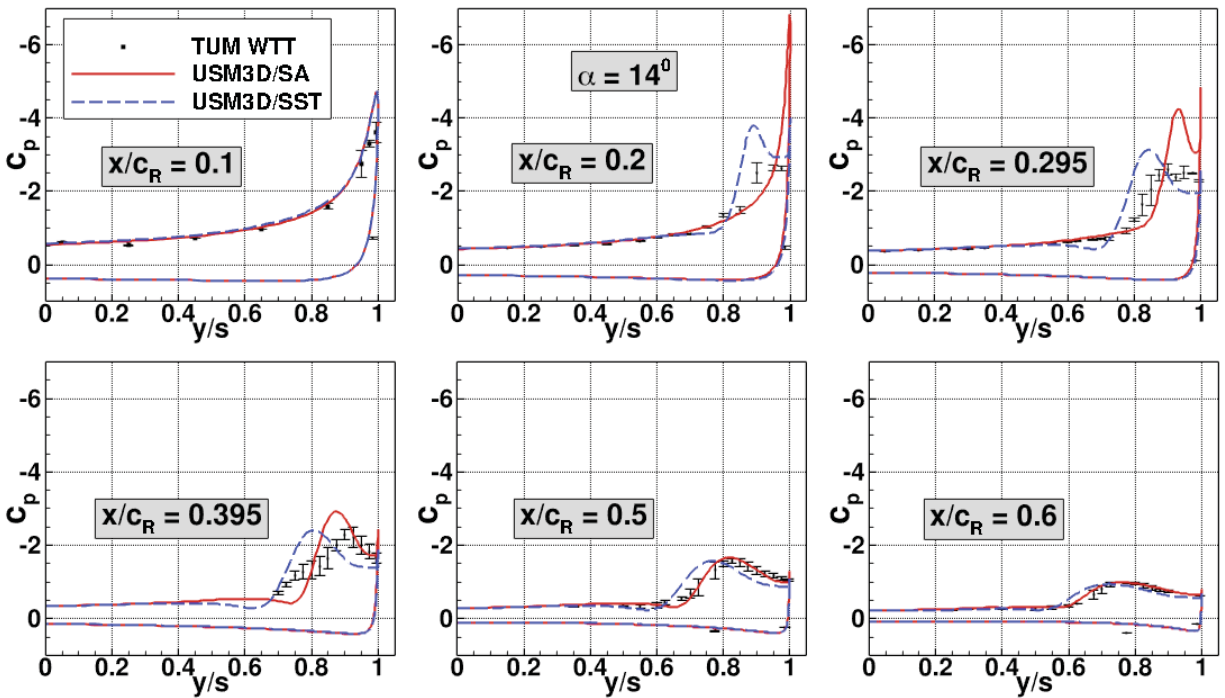
American Institute of Aeronautics and Astronautics

Figure A-3. Effect of turbulence models on spanwise C_p distributions. $\alpha = 13^0$, $M_\infty = 0.15$, $Re_{mac} = 2.7\text{x}10^6$.

Figure A-4. Effect of turbulence models on spanwise C_p distributions. $\alpha = 14^0$, $M_\infty = 0.15$, $Re_{mac} = 2.7\text{x}10^6$.
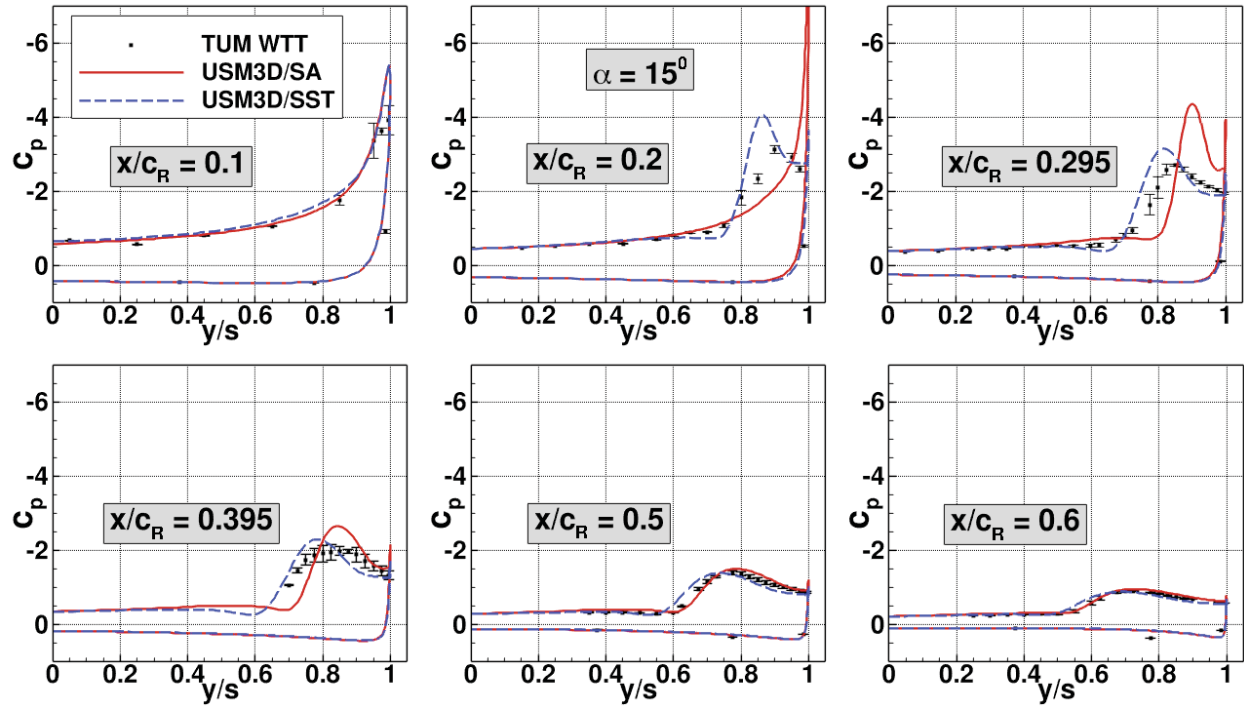
American Institute of Aeronautics and Astronautics

Figure A-5. Effect of turbulence models on spanwise C_p distributions. $\alpha=15^0$, $M_\infty=0.15$, $Re_{mac}=2.7x10^6$.